Quadrant Analysis of Turbulence in a Rectangular Cavity with Large Aspect Ratios

Dawei Guan[1]; Prakash Agarwal[2]; and Yee-Meng Chiew, M.ASCE[3]

Abstract: By using particle image velocimetry techniques, this paper presents new insights on the turbulence structure and time-averaged flows in a rectangular cavity with large aspect ratios. The three cavity aspect ratios (L/D, where L = cavity length, D = cavity depth) used in this study are 9.9, 13.0, and 18.9. The time-averaged velocity fields and Reynolds shear stress distributions within the cavity show that the flow pattern and turbulence structures are strongly affected by the cavity aspect ratio. The quadrant dynamic analysis of velocity fluctuations on the cavity shear layers and cavity downstream edge for the three cavities is conducted. Considering all of the bursting events with hole size parameter, H = 0 in the measured planes, sweeps are found to have the highest probability of occurrence within the zone of the shear layer, and ejections dominate almost all of the areas within the cavity and a certain depth of flow immediately above the shear layer. For the high-magnitude events (H = 1), quadrant dominances are almost inverted for all of the measured planes. The quadrant shear stress distributions show that the opposing events are approximately balanced for these regions on the cavity shear layers and along the cavity downstream edge.
DOI: 10.1061/(ASCE)HY.1943-7900.0001480.

Author keywords: Turbulence; Quadrant analysis; Particle image velocimetry (PIV); Rectangular Cavity; Large aspect ratio.

Introduction

Cavity flows have always presented great practical interests for engineers and researchers due to their various engineering applications, such as pollutant dispersion (Chang et al. 2007), flow energy exchanges (Botella and Peyret 1998), and sediment transport (Agarwal 2017; Lai et al. 2010). Extensive studies on the flow characteristics within an open cavity have been conducted in the past few decades, showing that the characteristics of cavity flows not only are related to the flow conditions such as flow compressibility, viscosity, free-stream velocity, flow depth, boundary layer thickness and turbulence levels (Chang et al. 2007; Immer et al. 2016; Rowley and Williams 2006), but are also sensitively dependent on the geometry of the cavity (Ozalp et al. 2010; Zhang and Hubert 2016). For cavities with small aspect ratios ($L/D < 5$, where L = cavity length, D = cavity depth), many studies conducted in either wind tunnels or open channels have experimentally and numerically shown that the flow within the cavity is characterized by large recirculation regions, and the associated shear layer only bridges the upstream and downstream edges of the cavity without sweeping into it (Botella and Peyret 1998; Erturk et al. 2005). For cavities with large aspect ratios ($L/D > 5$), however, the flow pattern within the cavities is significantly different from those in cavities with small aspect ratios; the shear layer developed at the cavity leading edge sweeps into the cavity, interacting with the recirculation region (Ukeiley and Murray 2005; Zdanski et al. 2006). For cavities with infinite lengths and finite depths (L/D approximately = ∞), the flow patterns near the cavity upstream and downstream edges can be separately regarded as a backward-facing step flow and a forward-facing step flow, respectively, as they cannot interact with each other. The characteristics of such typical step flows can be found in Spazzini et al. (2001) and Ren and Wu (2011). In addition, cavity flows, which are time and space dependent, consist of a complex array of evolving turbulent structures with different scales. This attribute greatly increases the challenge associated with the conduct of experimental works in quantifying the time- or phase-averaged cavity shear layers. Over the past few decades, the development of the particle image velocimetry (PIV) technique has made great contributions to the understanding of turbulence associated with cavity flows. By using the PIV technique, Ashcroft and Zhang (2005) studied the vortical structures over rectangular cavities and found that the size and growth rate of coherent vortical structures within the cavity vary with the geometry of the cavity. Amador et al. (2006) showed that the highest Reynolds shear stress region occurs near the adjacent step edges based on their study on the flow patterns and turbulence structures over consecutive triangular cavities. Ozalp et al. (2010) presented the turbulence structures of cavity flows within different cavity geometries (rectangular, triangular, and semicircular) and found that the rectangular and triangular cavities produce much greater turbulence compared with semicircular cavity geometry. Immer et al. (2016) conducted an experimental study on boundary layer thickness effects on flow fields over a unit–ratio cavity and concluded that the boundary layer thickness has little effect on the mean flow streamlines but significantly affects the formation of shear layer spanning the cavity top. However, these studies are confined to turbulent cavity flows with relatively small cavity aspect ratios ($L/D < 5$); limited published experimental data hitherto can be found on the characteristics of detailed turbulence structures in a rectangular cavity with large aspect ratios ($L/D > 5$). Because the aspect ratio has a significant effect on the complex nature of

[1]Lecturer, Key Laboratory of Coastal Disaster and Defense, Hohai Univ., Ministry of Education, Nanjing 210098, China; Research Fellow, School of Civil and Environmental Engineering, Nanyang Technological Univ., Singapore 639798. Email: david.guan@hhu.edu.cn

[2]Graduate Student, School of Civil and Environmental Engineering, Nanyang Technological Univ., Singapore 639798. Email: prakash005@e.ntu.edu.sg

[3]Professor, School of Civil and Environmental Engineering, Nanyang Technological Univ., Singapore 639798 (corresponding author). Email: cymchiew@ntu.edu.sg

Note. This manuscript was submitted on June 24, 2017; approved on January 4, 2018No Epub Date. Discussion period open until 0, 0; separate discussions must be submitted for individual papers. This paper is part of the ***Journal of Hydraulic Engineering***, © ASCE, ISSN 0733-9429.

turbulent cavity flows, it is both interesting and necessary to conduct detailed experimental studies on this topic. In the field, the bed of some streams or channels are paved with concrete blocks for the purpose of grade control, whose height/length ratios are commonly larger than 8. During the life span of these channels, some of the concrete blocks may be damaged or dislocated from their original position during floods, forming cavities with even larger aspect ratios. Therefore, the flow fields within these cavities are important for hydraulic engineers when a recalculation of the hydraulic conditions is needed.

Quadrant analysis, which is a simple but powerful turbulence data-processing technique, has been used widely in the investigation of complex turbulent shear flows (Dwivedi et al. 2010; Wallace 2016). By quantifying the magnitude and duration of turbulent velocity fluctuations in four quadrants, the spatially and temporally averaged turbulence structures of the flow can be better understood. This paper presents a detailed experimental examination of the contributions of the Reynolds shear stress in the streamwise x-z coordinate plane within three rectangular cavities with different (large) aspect ratios. Because the cavity length used in this study is large (1 m), the examination zones are only confined to the center (CS) and downstream corner sections (DS) of the cavities, corresponding to the two most interesting areas within the cavity for turbulence mixing and particle entrainment (Agarwal 2017; Lai et al. 2010). Agarwal (2017) found that entrainment of a particle from the cavity is closely related to the flow field at the center, because it dictates whether the particle will be swept upstream or downstream. Moreover, after reaching the downstream end of the cavity, actual entrainment of the particle is intimately connected to the local flow field at the edge of the cavity (Lai et al. 2010). From the viewpoint of particle entrainment from a large rectangular cavity, the flow field at these two locations is of primary importance.

Experiment and Methodology

Experimental Setup

The experiments were carried out in a 14-m-long, 0.60-m-deep, and 0.49-m-wide glass-sided recirculating flume in the Hydraulics Laboratory of Nanyang Technological University. The flume contains a 1-m-length by 0.49-m-width rectangular depth-adjustable cavity. The leading edge of the cavity is located 9 m downstream of the flume inlet. In this study, one constant cavity length, $L = 1$ m, and three cavity depths, $D = 5.3$, 7.7, and 10.1 cm (corresponding to three aspect ratios of 9.9, 13.0, and 18.9) were used to ensure a sufficient range of large aspect ratios. For all selected cavity sizes, the ratios of flume width and flow depth within the cavities are smaller than 5, signifying that secondary currents could be induced by the flume sidewalls within the cavities (Nezu and Nakagawa 1993). Therefore, flow measurements were conducted on the centerline of the flume to minimize sidewall effects. To obtain a fully developed turbulent flow, the flume floor was roughened with uniform sand of median grain size, $d_{50} = 0.36$ mm, throughout the flume length except for the cavity zone. A steady uniform approach flow with a constant depth of 12 cm and average velocity, $U = 26.0$ cm/s, were used in all of the tests. The corresponding Reynolds number ($\mathrm{R}_D = UD/v$, where h = upstream flow depth and ν = kinematic viscosity) of the approach flow is about 35,000. The corresponding Reynolds numbers based on cavity depths for the three cavities ($\mathrm{R}_D = UD/v$) are approximately 15,300, 22,200, and 29,200, respectively. The flow condition was examined before actual experimental works began by using both acoustic Doppler velocimeter and PIV measurements on the center of the flume, 1 m upstream of the cavity leading edge. The detailed experimental setup and calibration procedures can be found in Agarwal (2017).

Fig. 1 shows the PIV measurement sections, central section (CS), and downstream section (DS) within the cavity along the centerline of the flume. The flow fields within the rectangular cavities may be regarded as quasi-two-dimensional. The reference point $(x, z) = (0, 0)$ of the x-z coordinate plane in this study was set at the downstream cavity edge on the flume center (Fig. 1). The PIV system consisted of a 5-W diode-pumped solid-state continuous laser with a wavelength of 532 nm, and a high-speed camera (Phantom Miro 120, Vision Research, Wayne, New Jersey) with 3 GB of memory storage. The flow was seeded with polyamide tracer particles of diameter = 20 μm and specific gravity = 1.23 for optimal scattering of the laser light. Using Stroke's law, the settling velocity of the seeding particle was estimated to be 50.1 μm/s, which is negligible compared with the average approach flow velocity. The high-speed camera operated with a 50-mm focal lens at 150 frames per second. For each case, more than 6,000 images were measured. For the image processing, multiple interrogation windows (starting from 32×32 pixels, then passing with 16×16 pixels and ending with 8×8 pixels; all passes adopted a 50% overlap between adjacent subwindows) were adopted in the correlation algorithm to ensure the accuracy of the velocity calculation. Instead of using the traditional PIV imaging processing method with a fixed time interval Δt between two consecutive images, a multitime interval algorithm method developed by Hsieh et al. (2016) was adopted to reduce the bias error due to the high velocity gradient in the flow field. The multiple time intervals used are Δt (= 6.7 ms), 3, 9, and $21\Delta t$. This method also includes a digital image high-pass filter technique that was used to reduce reflections and scatterings of the laser light. The PIV data calculation was done with a series of FORTRAN codes, whose detailed procedures can be found in Hsieh (2008) and Hsieh et al. (2016). The maximum error of the instantaneous velocities was found to be about 3.4%. A convergence analysis was also conducted to ensure that the number of images in this study was enough to obtain a stable time-averaged turbulence data output. The experimental conditions are tabulated in Table 1, in which the letters and numerals in the "Measurement section" column

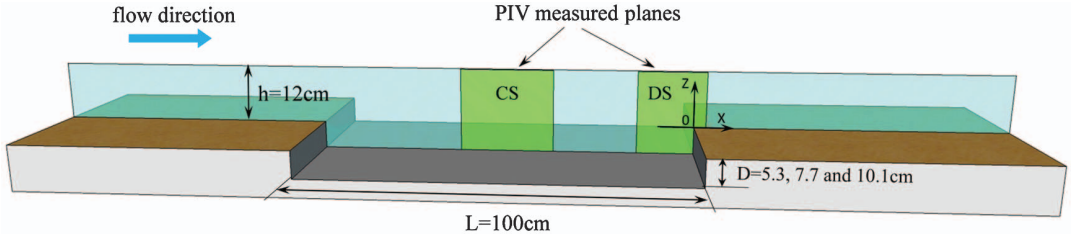

F1:1 **Fig. 1.** (Color) Sketch of cavity model and PIV measurement sections.

Table 1. Experimental conditions for PIV measurements

Measurement section	Field of view (cm^2)	Scale (cm/pixel)	Spatial resolution (cm)
CS053	26.0×15.3	0.01854	0.148
DS053	27.5×15.3	0.01886	0.151
CS077	28.5×19.7	0.01978	0.158
DS077	27.5×19.7	0.01961	0.157
CS101	20.0×22.1	0.02110	0.169
DS101	24.0×22.1	0.02109	0.169

(e.g., CS053) refer to the location of the measurement plane (center section) and depth of cavity (53 mm), respectively. The spatial resolution is calculated as the product of the minimum interrogation window (8 pixels) and the measurement scale.

Quadrant Analysis Methodology

Wallace et al. (1972) conducted the first quadrant analysis of Reynolds shear stresses in a turbulent shear flow at the wall region to explore the then-unknown information on turbulence from the signs of velocity fluctuations. In this study, the quadrant dynamics are locally affected by the cavity shear layers generated with different cavity aspect ratios. The turbulent events are designated according to the sign of the fluctuating velocity components. Therefore, the two-dimensional instantaneous turbulent velocity fluctuations (u', w') may be classified into four categories: Q1 $(+u', +w')$, Q2 $(-u', +w')$, Q3 $(-u', -w')$, and Q4 $(+u', -w')$, which are customarily called outward interaction, ejection, inward interaction and sweep events, respectively. As indicated in Pope (2000), Reynolds shear stress is expressed as $-\langle u'w' \rangle$ and the turbulence production is calculated as $T_P = -\langle u'w' \rangle (\partial u/\partial z)$; therefore, Q1 and Q3 give negative contributions to the Reynolds shear stress and lead to energy dissipation, whereas Q2 and Q4 give positive contributions to the Reynolds shear stress and result in energy production. To differentiate the higher magnitude contributions to the time-averaged Reynolds shear stress $-\overline{u'w'}$ from each quadrant, a hole-size parameter H is adopted (Nezu and Nakagawa 1993; Willmarth and Lu 1972). The hyperbolic hole area is determined by the curve $|u'w'| = H(u'_{\text{rms}} w'_{\text{rms}})$, in which u'_{rms} and w'_{rms} and are the root mean square of the horizontal and vertical instantaneous turbulent velocity fluctuations, respectively. With an increase in H, the hole area is enlarged and the fractional contribution of the remaining data outside of the hole to the total shear stress can be determined. Thus, the shear stress fraction from each quadrant can be written as

$$S^f_{i,H} = \langle u'w' \rangle_{i,H} / \overline{u'w'} \tag{1}$$

where $\langle u'w' \rangle_{i,H}$ are the contributions from the ith quadrant to $-\overline{u'w'}$, and is calculated as

$$\langle u'w' \rangle_{i,H} = \sum_{n=1}^{N} u'(n) w'(n) I_{i,H}(u', w') \tag{2}$$

and N = number of total bursting events; n = number of instantaneous bursting events; and $I_{i,H}(u', w')$ = detection function, defined as

$$I_{i,H}(u', w') = \begin{cases} 1, & if\ (u', w')\ is\ in\ qudrant\ i\ and\ if\ |u'w'| \geq H(u'_{\text{rms}} w'_{\text{rms}}) \\ 0, & otherwise \end{cases} \tag{3}$$

The duration fraction $T^f_{i,H}$ for the ith quadrant is defined as

$$T^f_{i,H} = \frac{1}{N} \sum_{n=1}^{N} I_{i,H}(u', w') \tag{4}$$

The conditional statistics of experimental data of the Reynolds shear stress within the cavity flow are analyzed using these equations.

Results and Discussion

Time-Averaged Velocity and Reynolds Shear Stress Distributions

The time-averaged velocity and normalized Reynolds shear stress $(-\overline{u'w'}/U^2)$ distributions of the measured sections are shown in Fig. 2. First, the experimental data show that the flow fields of the regions above $Z = -5$ cm in all three cavities with different aspect ratios are generally similar. For the largest cavity depth with $D = 10.1$ cm, an obvious flow recirculation zone can be identified at the downstream corner of the cavity (see DS101 in Fig. 2). Second, although only two sections (one at the center and the other at the downstream edge of the cavity) of the entire cavity flow field were measured in this study, one still can readily infer from the experimental data how a well-developed strong positive Reynolds shear stress layer (indicated by the belt of dark red color in the regions of -60 cm $< X < -40$ cm, and -3 cm $< Z < 2$ cm of the CS sections in Fig. 2) that forms at the cavity leading edge has swept into the cavity and reattached onto the cavity floor. It then separates before reaching the downstream cavity wall to rejoin the main flow there. This is consistent with the observed flow patterns within a large aspect ratio ($L/D = 5.16$) cavity by other researchers (Ukeiley and Murray 2005). In compressible cavity flows, such a flow regime is defined as a *closed* cavity flow (Plentovich et al. 1993); it occurs in very shallow cavities with aspect ratios greater than 9 (Ashcroft and Zhang 2005). Third, the values of the normalized time-averaged Reynolds shear stress of all the cases are very small and fluctuate around zero above the strong positive shear stress layer. This is due to the unsteady small vertical velocity gradients. Fourth, Fig. 2 also reveals that a strong negative Reynolds shear stress zone is formed immediately downstream of the cavity downstream edge due to contraction of the flow cross section for all three cases. Moreover, the time-averaged flow and turbulence structure at the cavity downstream edge are found to be similar to those on a forward-facing step (Ren and Wu 2011). This is because, for a cavity with large aspect ratios, the flow can reattach onto the bottom of the cavity and redevelop to a quasi-uniform state before reaching the downstream cavity edge. However, to determine a critical aspect ratio that renders cavity flows to resemble that with a forward-facing step still needs further study. Finally, the increase of cavity depth increases the magnitude of the positive Reynolds shear stress layer within the cavity and the negative Reynolds stress zone immediately upstream of the cavity downstream edge.

Velocity Fluctuations

Fig. 3 shows quadrant maps of the fluctuating component of velocity u' and w' at selected locations for Tests CS077 and DS077. Instead of a direct presentation of scatter plots, the data have been contoured in terms of probability density and normalized by the cavity upstream approach average velocity for a better comparison. Therefore, the plots in Fig. 3 are joint probability distribution functions (PDFs) of the two fluctuating components of velocities

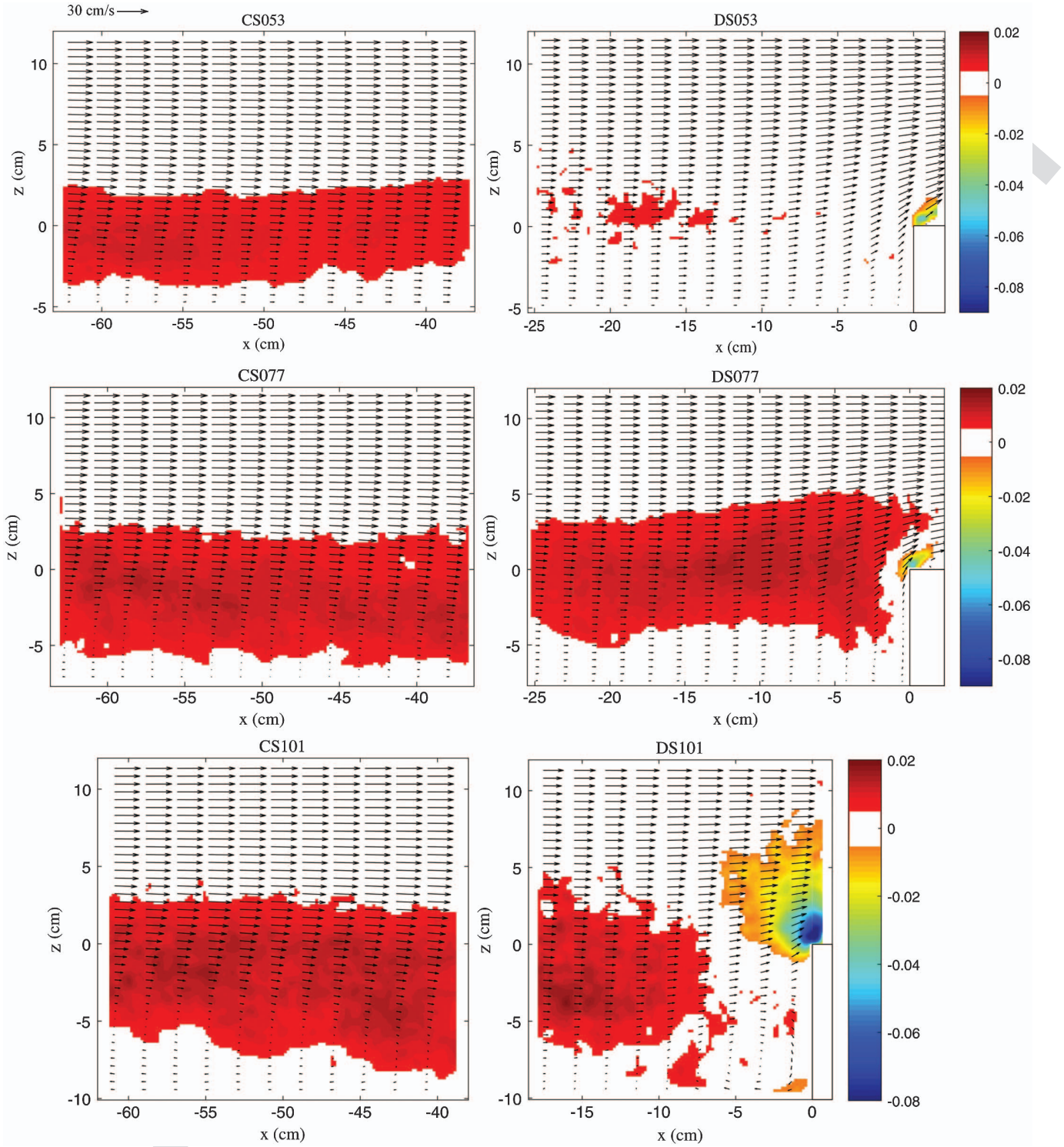

F2:1 **Fig. 2.** (Color) Time-averaged velocity vectors and normalized Reynolds shear stress distributions (the color scale represents the magnitude of
F2:2 normalized Reynolds shear stress $-\overline{u'w'}/U^2$; flows from left to right).

u' and w'. The joint probability of the paired velocity fluctuations $P(u', w')$ in a given region in the u'-w' plane can be calculated based on the occurrence numbers of the instantaneous velocity fluctuations over the region. The darkest zones in each plot correspond to the largest concentrations of instantaneous fluctuations for that position. Moreover, the sizes and shapes of the joint PDFs at different locations indicate different turbulence properties. A careful examination of the data at locations [Figs. 3(c, f, and i) on the right column of the figure] along the cavity top ($Z = 0$ cm) reveals that the velocity fluctuations have a similar turbulence intensity and appear as an elliptical shape, with their major axis skews into the Q2 and Q4 quadrants. This is consistent with the strong positive Reynolds shear stresses and the most frequent ejections and sweep events that form at these locations (Fig. 2). On the cavity center and above the cavity top, however, the major axis of the elliptical joint PDF reduces its length and rotates anticlockwise as Z increases [Figs. 3(a–c), top row], indicating a reduced turbulent-like behavior. On the cavity center and within the cavity ($Z < 0$), strong

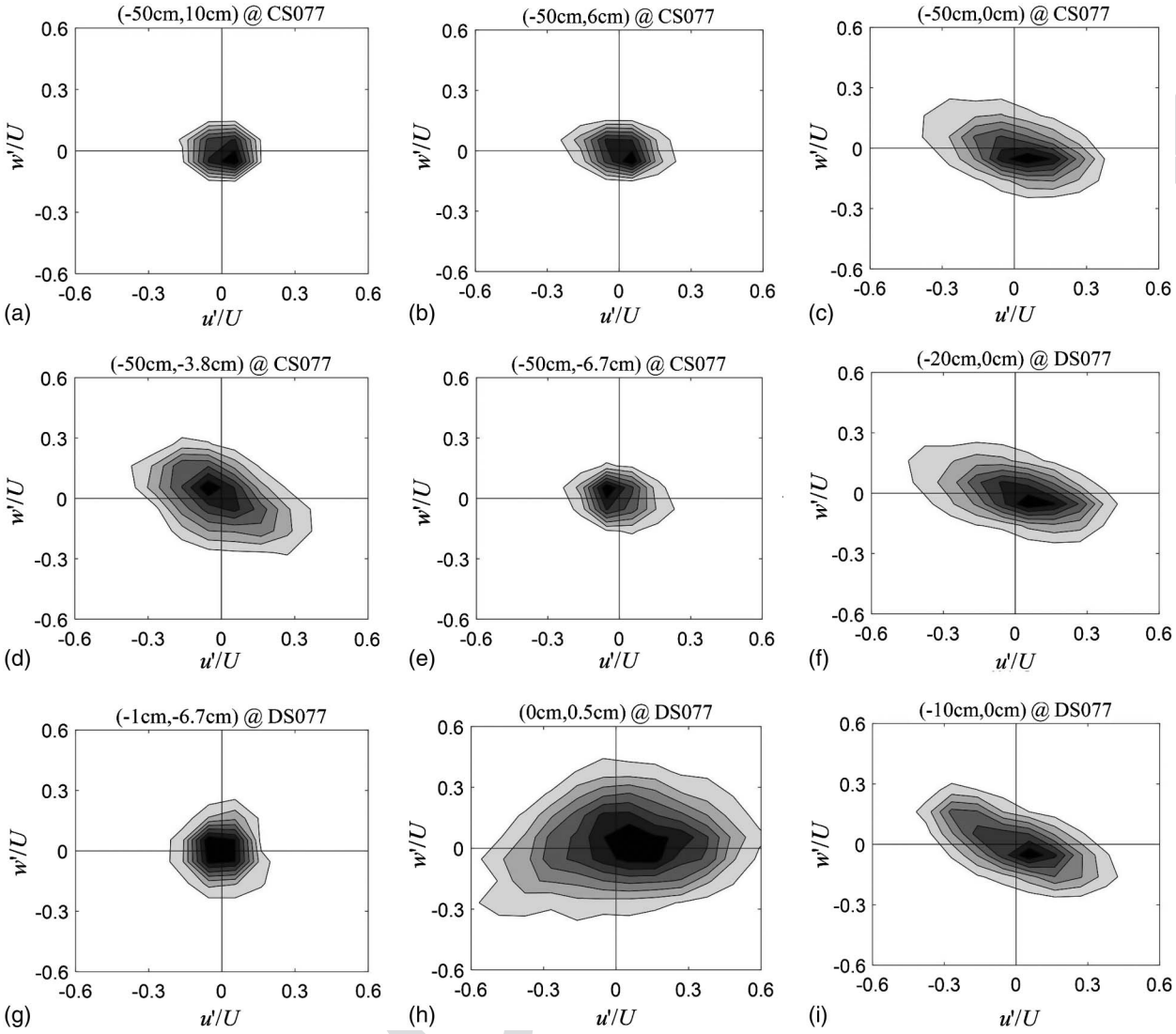

F3:1 **Fig. 3.** Joint PDFs of normalized velocity fluctuations u' and w' at specific locations for Tests CS077 and DS077 (coordinates of the locations are
F3:2 shown on the top of each subplot).

velocity fluctuations still can be observed within the band of positive Reynolds shear stress layer [Fig. 3(d)]. The small joint PDF of Fig. 3(e) (1 cm above the center of the cavity floor) shows that the turbulence is restricted near the cavity floor. At the downstream corner (−1 cm, −6.7 cm) of the cavity [Fig. 3(g)], a symmetrical distribution (circular) of joint PDF is observed. This indicates that the turbulence is small and nearly isotropic at this location. Immediately above the downstream cavity edge [Fig. 3(h)], the distribution of velocity fluctuations also adopts an elliptical shape, but with its major axis skewed into the Q1 and Q3 quadrants. The largest size of PDF (of all the subplots) at this location indicates its strongest turbulence intensity in the measured planes. This is a reflection of the strongest negative Reynolds shear stress developed at this location (Fig. 2).

Dominant Quadrant Event Distributions

For a specific hole-size H, the dominant quadrant of the highest probability of occurrence at a given location is obtained by comparing the magnitude of the duration fractions $T^f_{i,H}$. The dominant quadrant event distributions of the measured sections are shown in Fig. 4. Two hole sizes, $H = 0$ and 1, are used in this part of the analysis. The events associated with Q2 and Q4 are the most frequent in the measured flow field for all three cases. For $H = 0$, the results associated with the three center sections (CS053, CS077, and CS101) show a similar pattern of dominant quadrant distribution within and below the cavity shear layer (indicated as the strong positive Reynolds shear stress layers in Fig. 2; see the regions of -60 cm $< x < -40$ cm, and -3 cm $< Z < 2$ cm). Specifically, Q4 has the highest probability of occurrence within the zone of the shear layer, and Q2 almost dominates all areas within the cavity and a certain depth of flow immediately above the shear layer. This feature is consistent with previous works in stepped cavity flows (e.g., Amador et al. 2006). For the flow layers above the cavity shear layer, the dominant quadrant distributions are different for the three different cases. As mentioned in the previous section, the reattached position of the shear layer is strongly dependent on the cavity aspect ratios. Therefore, it can be inferred that (1) the downstream shift and progressive enlargement of the Q1 region associated with the small negative time-averaged Reynolds shear stresses (Fig. 2), and (2) the reducing dominance of the Q2 region above the cavity shear layer in CS077 and CS101, are closely related to the decrease of the cavity aspect ratio.

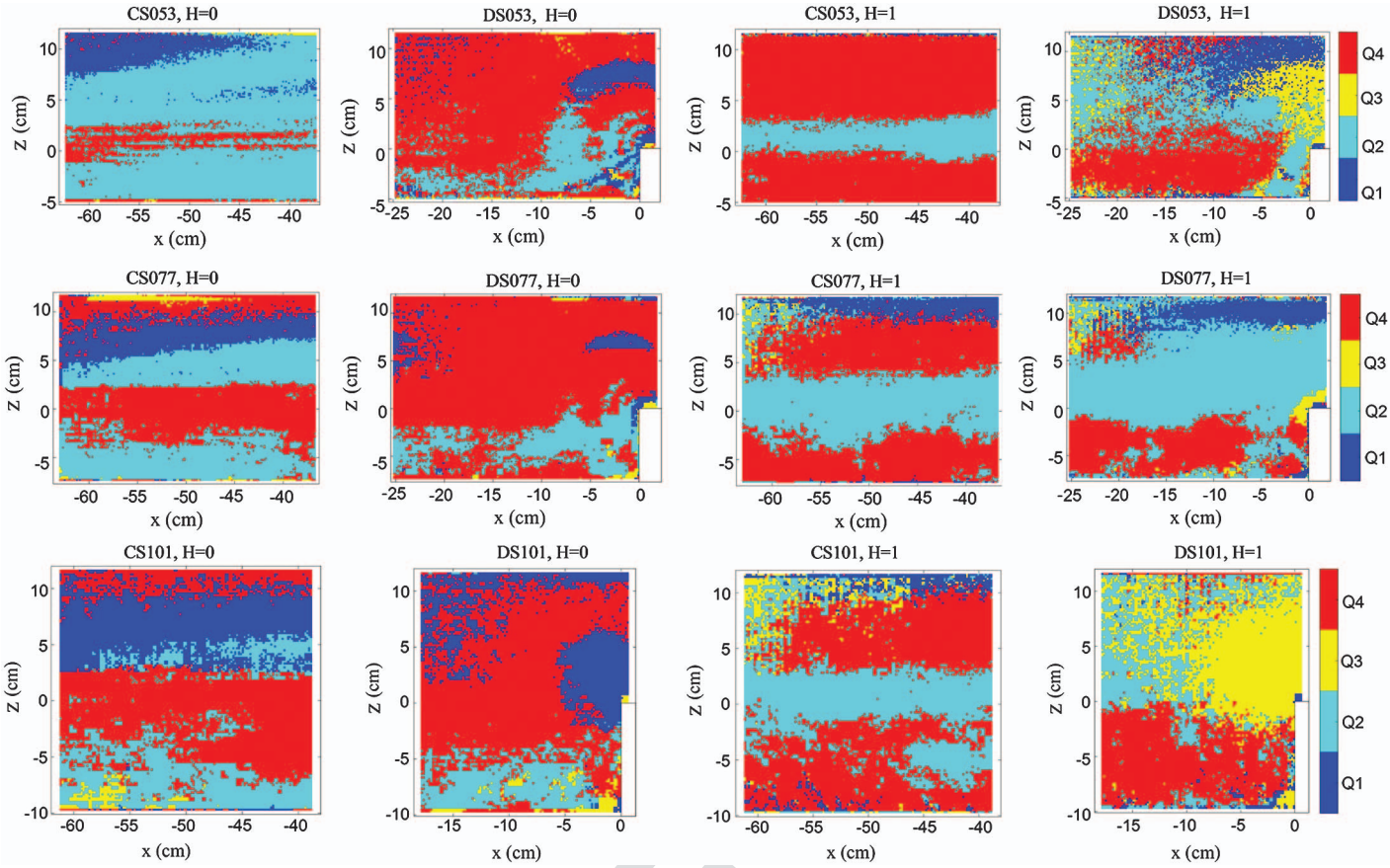

F4:1 **Fig. 4.** (Color) Dominant quadrant event distribution of measured sections.

For $H = 0$, Q4 dominates almost all flow areas above the cavity, and Q2 is the most frequent event within the cavity in all three downstream sections (DS053, DS077, and DS101). Q1 and Q3 have higher occurrences at the cavity corners and around the cavity downstream edge, which corresponds to the areas with negative Reynolds shear stresses. For the high-magnitude events ($H = 1$), quadrant dominances are almost inverted for all measured planes. This feature, which is consistent with the findings in Amador et al. (2006), indicates an asymmetry of high infrequent velocity fluctuations. Although these patterns of quadrant maps in Fig. 4 appear to be clear, an erroneous interpretation is possible because of a slight dominance from specific events (Buffin-Bélanger and Roy 1998).

Quadrant Shear Fractions

Fig. 5 shows the profiles of fractional Reynolds shear stress contributions, $S^f_{i,H}$, for $H = 0$ at different locations along the measured sections. Clearly, the cavity aspect ratio has a significant effect on the distributions of the quadrant shear fractions because of its influence in modifying the flow structures within the cavity. Although the distributions of shear fractions for all three cases are not identical, some common properties still can be deduced from Fig. 5. For the regions having high absolute time-averaged Reynolds shear stress values, such as regions of the cavity shear layer and around the cavity downstream edge, the absolute values of contribution fractions for all quadrants are within a small range from 0 to 1.5. These small Reynolds shear stress fractions provide an interesting feature, indicating that the opposing events are approximately balanced. For the rest of the regions having small absolute time-averaged Reynolds shear stress values, the absolute values of contribution fractions are within a relatively larger range from 1.5 to 4. In these regions, Q2 and Q3 are found to be the dominant contributions among the opposing events. A cursory comparison with Fig. 3 reveals that these regions have the highest occurrence probability of Q1 and Q4. These contrasting observations indicate that a larger proportion of the shear stress is generated over shorter durations. In a previous study on transition boundary layers, similar observations were found by Nolan et al. (2010).

To further investigate the high-magnitude quadrant events on the cavity shear layers, the fractional Reynolds shear stress contributions against hole size H at three locations [(−50 cm, 0 cm), (−10 cm, 0 cm), and (0 cm, 0.5 cm)] are plotted in Fig. 6. The dash curve T in the plots represents the percentage of time that the data are outside the hole with a certain value of H. For all locations in the three cases and $H = 2$, Fig. 6 shows that the motions outside of the hole occur less than 5% of the total time, whereas the total Reynolds shear stress results from all these motions still account for considerable proportions. This behavior indicates that the high intense, intermittent motions are the major source of Reynolds stress. For the two locations within the cavities, Q2 and Q4 are the dominant positive contributions to the total Reynolds shear stresses, whereas for the locations on the cavity's downstream edge, Q1 and Q3 are the dominant positive contributions. This is consistent with the signs of the total Reynolds shear stresses at these locations observed in Fig. 2. The balancing feature of the opposing events at locations with high absolute time-averaged Reynolds shear stresses is sustained and asymptote to a constant value of zero as the hole size increases [Figs. 6(a, c, e, f, and i)]. This feature indicates an evenly distributed elliptical or circular shape of velocity fluctuations on the quadrant map. Figs. 6(c, f, and i) also indicate that, for the

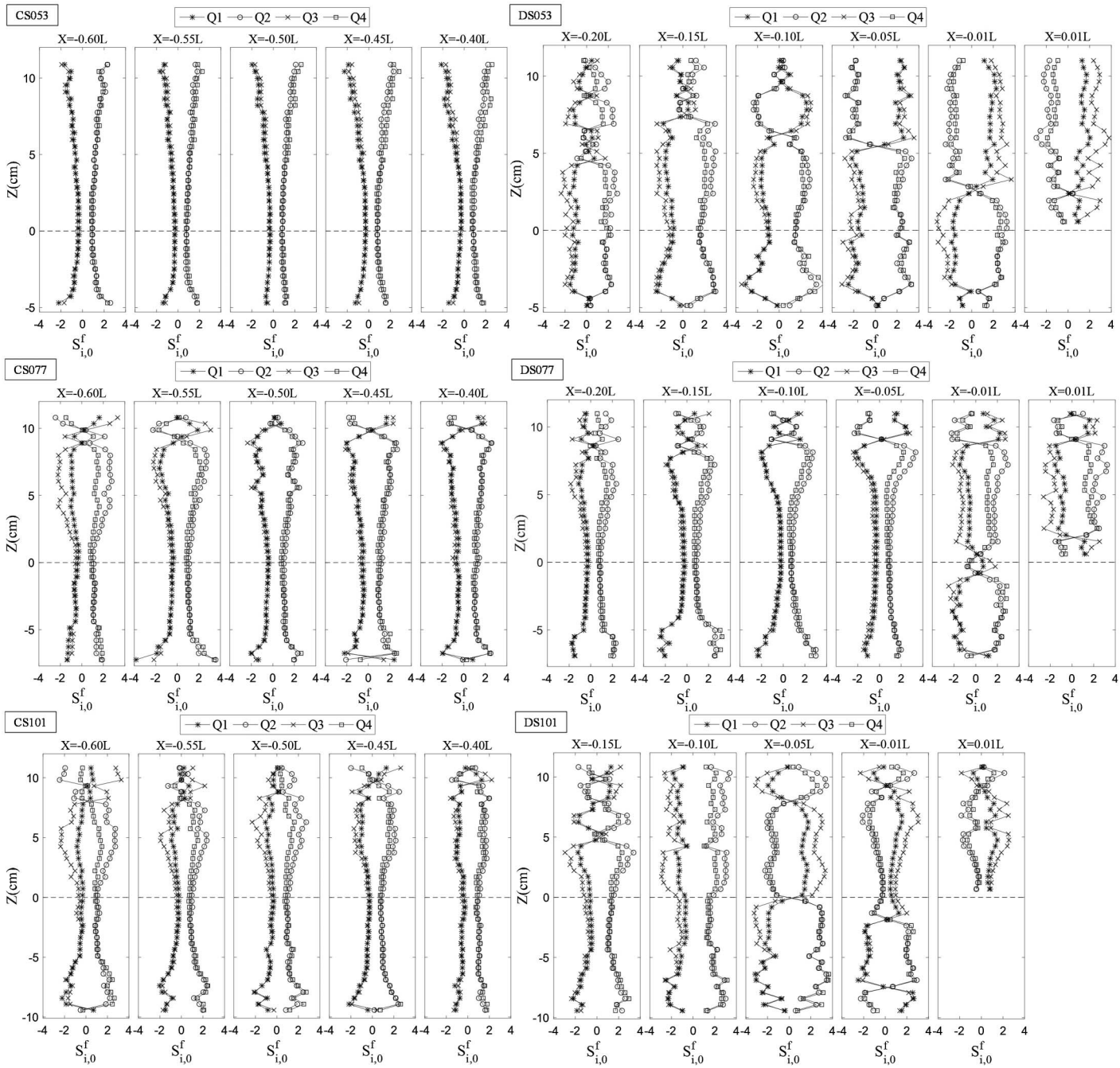

F5:1 **Fig. 5.** Vertical profiles of quadrant shear fractions, $S^f_{i,0}$, along the measured planes for the three cavities (locations of vertical profiles are shown on
F5:2 top of each subplot).

locations with larger Reynolds shear stress, all contributions from the four quadrants vanish quicker with an increase of the hole size.

Conclusions

This paper presents an experimental study on the quadrant analysis of turbulence structures in a rectangular cavity with comparatively large aspect ratios using a high spatial resolution PIV technique. New insights on the turbulence structures of the time-averaged flow within the cavity of large aspect ratios are presented. The measured time-averaged velocity field and Reynolds shear stress distributions within the cavity show that the flow pattern and turbulence structures are strongly affected by the cavity aspect ratio. With an increase of the cavity depth, the negative Reynolds shear stress region at the cavity's downstream edge increases its intensity in both magnitude and extent. For $H = 0$, the dominant quadrant event distributions of all three cavity sizes show a similar feature (i.e., Q4 has the highest probability of occurrence within the zone of the shear layer, and Q2 dominates almost all areas within the cavity and a certain depth of flow immediately above the shear layer). For $H = 1$, quadrant dominances in all cavity sizes are inverted. The quadrant shear stress distributions show that the opposing events are approximately balanced on the cavity shear layers and near the cavity's downstream edge. This balanced feature indicates an evenly distributed elliptical or circular shape of velocity fluctuations on the quadrant map. The quadrant hole analysis for locations on the cavity shear layers reveals that the percentage of

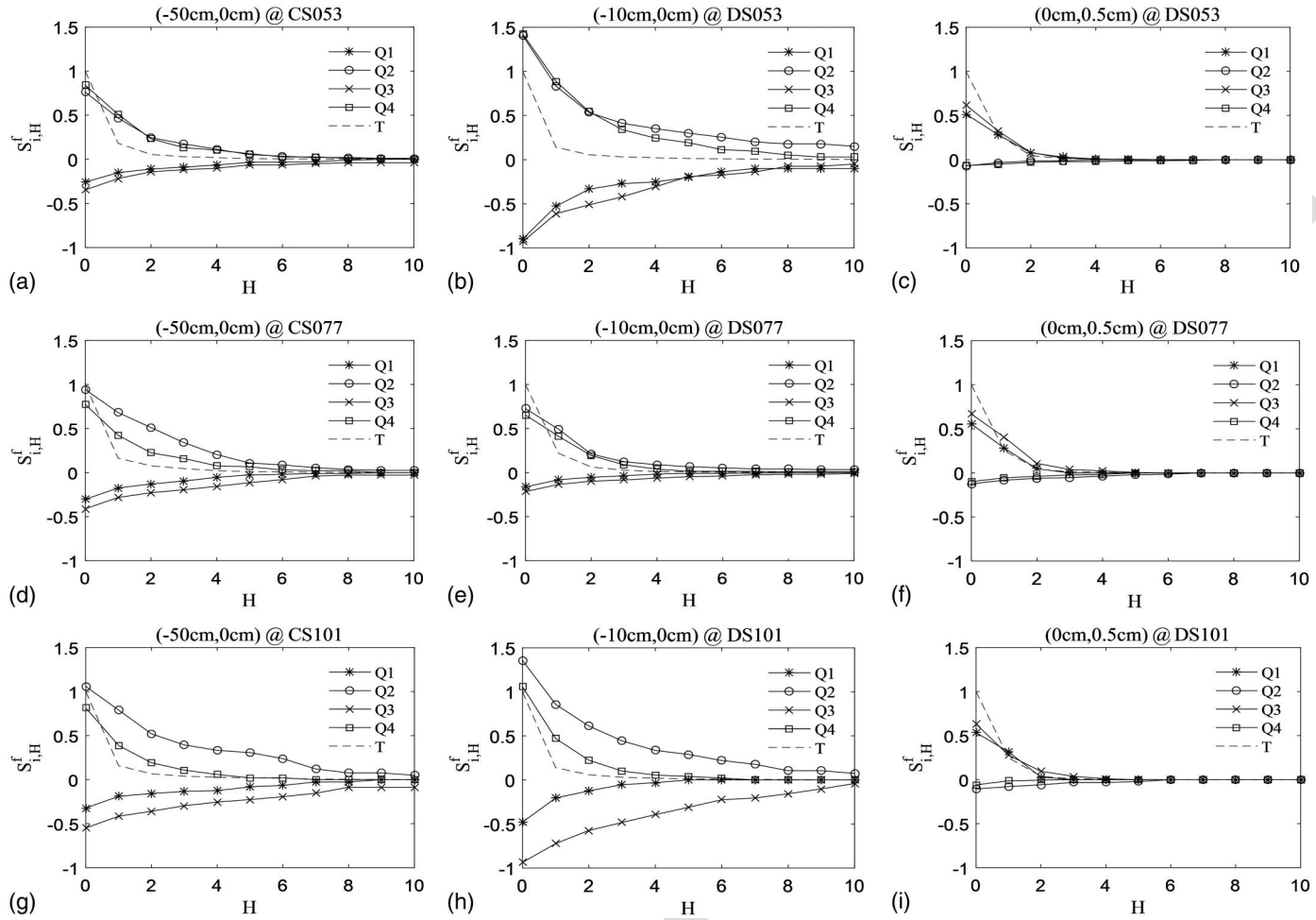

F6:1 F6:2 **Fig. 6.** Fractional contributions to Reynolds shear stress, $S^f_{i,H}$, at noted locations as a function of H (coordinates of the locations are shown on top of each subplot; T represents the percentage of time that the data are outside of the hole, and uses the same vertical scale as $S^f_{i,H}$).

time that the motions are outside of the hole drops much quicker than those of the shear fractions. This indicates that small periods of strong velocity fluctuations contribute large proportions to the total Reynolds shear stress at these locations. Finally, the present experimental results of this study will be useful in the turbulence modeling of cavity flows.

Acknowledgments

The authors sincerely thank Dr. S. C. Hsieh for his significant contributions to the development of the PIV data processing algorithm. The NTU Research Scholarship provided by Nanyang Technological University to the second author is gratefully acknowledged. This research was supported by the Young Scientists Fund of the National Natural Science Foundation of China (51709082).

Notation

The following symbols are used in this paper:

D = cavity depth (m);
d_{50} = median sediment size (m);
H = hole size;
h = approach flow depth (m);
$I_{i,H}$ = detection function;
i = quadrant numbers (i.e., 1, 2, 3, 4);
L = cavity length (m);
N = number of total bursting events;
n = number of instantaneous bursting events;
Q1 = outward interaction events;
Q2 = ejection events;
Q3 = inward interaction events;
Q4 = sweep events;
R_D = Reynolds number based on cavity depth;
R_e = Reynolds number of the approach flow;
$S^f_{i,H}$ = shear stress fraction for the ith quadrant within the hole size H;
T = percentage of time that the data are outside of the hole;
$T^f_{i,H}$ = duration fraction for the ith quadrant within the hole size H;
T_P = energy production (m^2/s^3);
U = upstream average velocity (m/s);
u' = horizontal instantaneous turbulent velocity fluctuations (m/s);
u'_{rms} = root mean square of horizontal instantaneous turbulent velocity fluctuations (m/s);
ν = viscosity of water (m^2/s);
w' = vertical instantaneous turbulent velocity fluctuations (m/s);

w'_{rms} = root mean square of vertical instantaneous turbulent velocity fluctuations (m/s);

Δt = time interval between the two consecutive images (s);

$-\langle u'w' \rangle$ = instantaneous Reynolds shear stress (m^2/s^2);

$-\overline{u'w'}$ = time-averaged Reynolds shear stress (m^2/s^2); and

$\langle u'w' \rangle_{i,H}$ = contributions from the ith quadrant to $-\overline{u'w'}$ (m^2/s^2).

References

Agarwal, P. 2017. "Particle entrainment from a rectangular cavity in turbulent open-channel flows." Ph.D. thesis, Nanyang Technological Univ.

Amador, A., M. Sa, Sánchez-Juny, and J. Dolz. 2006. "Characterization of the nonaerated flow region in a stepped spillway by PIV." *J. Fluids Eng.* 128 (6): 1266–1273. https://doi.org/10.1115/1.2354529.

Ashcroft, G., and X. Zhang. 2005. "Vortical structures over rectangular cavities at low speed." *Phys. Fluids.* 17 (1): 015104. https://doi.org/10.1063/1.1833412.

Botella, O., and R. Peyret. 1998. "Benchmark spectral results on the lid-driven cavity flow." *Comput. Fluids.* 27 (4): 421–433. https://doi.org/10.1016/S0045-7930(98)00002-4.

Buffin-Bélanger, T., and A. G. Roy. 1998. "Effects of a pebble cluster on the turbulent structure of a depth-limited flow in a gravel-bed river." *Geomorphology.* 25 (3–4): 249–267. https://doi.org/10.1016/S0169-555X(98)00062-2.

Chang, K., G. Constantinescu, and O. P. Seung. 2007. "Purging of a neutrally buoyant or a dense miscible contaminant from a rectangular cavity. II: Case of an incoming fully turbulent overflow." *J. Hydraul. Eng.* 133 (4), 373–385. https://doi.org/10.1061/(ASCE)0733-9429(2007)133:4(373).

Dwivedi, A., B. Melville, and A. Y. Shamseldin. 2010. "Hydrodynamic forces generated on a spherical sediment particle during entrainment." *J. Hydraul. Eng.* 136 (10), 756–769. https://doi.org/10.1061/(ASCE)HY.1943-7900.0000247.

Erturk, E., T. C. Corke, and C. Gökçöl. 2005. "Numerical solutions of 2-D steady incompressible driven cavity flow at high Reynolds numbers." *Int. J. Numer. Methods Fluids.* 48 (7): 747–774. https://doi.org/10.1002/fld.953.

Hsieh, S. C. 2008. "Establishment of high time-resolved PIV system with application to the characteristics of a near wake flow behind a circular cylinder." Ph.D. thesis, National Chung Hsing Univ.

Hsieh, S. C., Y. M. Low, and Y. M. Chiew. 2016. "Flow characteristics around a circular cylinder subjected to vortex-induced vibration near a plane boundary." *J. Fluids Struct.* 65: 257–277. https://doi.org/10.1016/j.jfluidstructs.2016.06.007.

Immer, M., J. Allegrini, and J. Carmeliet. 2016. "Time-resolved and time-averaged stereo-PIV measurements of a unit-ratio cavity." *Exp. Fluids.* 57 (6): 101. https://doi.org/10.1007/s00348-016-2186-9.

Lai, J., S. Tsung, Y. M. Chiew, and F. Lee. 2010. "Gap scour at a stepped concrete block grade control structure." In *Scour and Erosion 2010 (ICSE-5)*, 619–628. San Francisco: ASCE.

Nezu, L., and H. Nakagawa. 1993. *Turbulence in open-channel flows*. Rotterdam, Netherland: A.A. Balkema.

Nolan, K. P., E. J. Walsh, and D. M. McEligot. 2010. "Quadrant analysis of a transitional boundary layer subject to free-stream turbulence." *J. Fluid Mech.* 658: 310–335. https://doi.org/10.1017/S0022112010001758.

Ozalp, C., A. Pinarbasi, and B. Sahin. 2010. "Experimental measurement of flow past cavities of different shapes." *Exp. Thermal Fluid Sci.* 34 (5): 505–515. https://doi.org/10.1016/j.expthermflusci.2009.11.003.

Plentovich, E. B., R. L. J. Stallings, and M. B. Tracy. 1993. *Experimental cavity pressure measurements at subsonic and transonic speeds static-pressure results*. NASA Technical Paper 3358, NASA Langley Research Center.

Pope, S. B. 2000. *Turbulent flows*. Cambridge, UK: Cambridge University Press.

Ren, H., and Y. Wu. 2011. "Turbulent boundary layers over smooth and rough forward-facing steps." *Phys. Fluids.* 23 (4): 045102. https://doi.org/10.1063/1.3576911.

Rowley, C. W., and D. R. Williams. 2006. "Dynamics and control of high-Reynolds-number flow over open cavities." *Ann. Rev. Fluid Mech.* 38 (1): 251–276. https://doi.org/10.1146/annurev.fluid.38.050304.092057.

Spazzini, P. G., G. Iuso, M. Onorato, N. Zurlo, and G. M. Di Cicca. 2001. "Unsteady behavior of back-facing step flow." *Exp. Fluids.* 30 (5): 551–561. https://doi.org/10.1007/s003480000234.

Ukeiley, L., and N. Murray. 2005. "Velocity and surface pressure measurements in an open cavity." *Exp. Fluids.* 38 (5): 656–671. https://doi.org/10.1007/s00348-005-0948-x.

Wallace, J. M. 2016. "Quadrant analysis in turbulence research: History and evolution." *Ann. Rev. Fluid Mech.* 48 (1): 131–158. https://doi.org/10.1146/annurev-fluid-122414-034550.

Wallace, J. M., H. Eckelmann, and R. S. Brodkey. 1972. "The wall region in turbulent shear flow." *J. Fluid Mech.* 54 (1): 39–48. https://doi.org/10.1017/S0022112072000515.

Willmarth, W. W., and S. S. Lu. 1972. "Structure of the Reynolds stress near the wall." *J. Fluid Mech.* 55 (1): 65–92. https://doi.org/10.1017/S002211207200165X.

Zdanski, P. S. B., M. A. Ortega, and N. G. C. R. Fico, Jr. 2006. "On the flow over cavities of large aspect ratio: A physical analysis." *Int. Commun. Heat Mass Transfer.* 33 (4): 458–466. https://doi.org/10.1016/j.icheatmasstransfer.2006.01.007.

Zhang, G., and C. Hubert. 2016. "Gabion stepped spillway: Interactions between free-surface, cavity, and seepage flows." *J. Hydraul. Eng.* 142 (5): 06016002. https://doi.org/10.1061/(ASCE)HY.1943-7900.0001120.

Queries

1. Please provide the ASCE Membership Grades for the authors Dawei Guan and Prakash Agarwal who are members.

2. Please check and confirm whether the authors' affiliations have been set correctly.

3. [ASCE Open Access: Authors may choose to publish their papers through ASCE Open Access, making the paper freely available to all readers via the ASCE Library website. ASCE Open Access papers will be published under the Creative Commons-Attribution Only (CC-BY) License. The fee for this service is $1750, and must be paid prior to publication. If you indicate Yes, you will receive a follow-up message with payment instructions. If you indicate No, your paper will be published in the typical subscribed-access section of the Journal.]

4. Please check the hierarchy of section heading levels.

5. Please provide issue id for reference Hsieh et al. (2016).

6. Please provide issue id for reference Nolan et al. (2010).

7. Please provide the publisher's location for reference Plentovich et al. (1993).